

Strong-field control of plasmonic properties in core-shell nanoparticles

Jeffrey Powell,^{1,2,3,*} Jianxiong Li,^{1,4,*} Adam Summers,^{1,5} Seyyed Javad Robotjazi,¹ Michael Davino,² Philipp Rupp,⁶ Erfan Saydanzad,¹ Christopher M. Sorensen,⁷ Daniel Rolles,¹ Matthias F. Kling,^{6,8} Carlos Trallero-Herrero,^{1,2} Uwe Thumm,¹ and Artem Rudenko¹

¹*J. R. Macdonald Laboratory, Department of Physics,
Kansas State University, Manhattan, Kansas 66506, USA*

²*Department of Physics, University of Connecticut, Storrs, Connecticut 06269, USA*

³*INRS, Énergie, Matériaux et Télécommunications,
1650 Bld. Lionel Boulet, Varennes, Québec, J3X1S2, Canada*

⁴*Department of Physics and Astronomy, Louisiana State University, Baton Rouge, Louisiana 70803, USA*

⁵*ICFO - Institut de Ciències Fotoniques, The Barcelona Institute
of Science and Technology, 08860 Castelldefels (Barcelona), Spain*

⁶*Physics Department, Ludwig-Maximilians-Universität Munich, D-85748 Garching, Germany*

⁷*Department of Physics, Kansas State University, Manhattan, Kansas 66506, USA*

⁸*Max Planck Institute of Quantum Optics, D-85748 Garching, Germany*

(Dated: August 17, 2021)

The strong-field control of plasmonic nanosystems opens up new perspectives for nonlinear plasmonic spectroscopy and petahertz electronics. Questions, however, remain regarding the nature of nonlinear light-matter interactions at sub-wavelength spatial and ultrafast temporal scales. Addressing this challenge, we investigated the strong-field control of the plasmonic response of Au nanoshells with a SiO₂ core to an intense laser pulse. We show that the photoelectron energy spectrum from these core-shell nanoparticles displays a striking transition between the weak and strong-field regime. This observed transition agrees with the prediction of our modified Mie-theory simulation that incorporates the nonlinear dielectric nanoshell response. The demonstrated intensity-dependent optical control of the plasmonic response in prototypical core-shell nanoparticles paves the way towards ultrafast switching and opto-electronic signal modulation with more complex nanostructures.

The ability to reversibly manipulate the electronic structure and optical response of nanometer-sized materials has recently attracted substantial attention [1–3]. A hallmark property of nanostructures is the capacity to design and fabricate systems to take advantage of the tunable, size-, shape-, frequency-, and material-dependent properties as a means of tailoring specific optical responses. This holds the promise to both further our understanding of the transient electronic response in solid matter as well as enable new applications such as novel opto-electronics [3], plasmonically enhanced light harvesting [4], and photocatalysis [5, 6]. Among different configurations, composite nanostructures, such as core-shell nanoparticles, consisting of a dielectric core and a thin metallic shell, are of special interest for their exceptionally large plasmonic field enhancements and high tunability of absorption spectra [7, 8], generating novel applications in optical imaging and photothermal cancer therapy [9, 10]. Precise control of the optical response, typically achieved by manipulating the geometric structures [8], is the key to utilizing their unique plasmonic properties.

Investigations into such optical properties in nanostructures have been conducted by studying their plasmonic response, in particular, their plasmonic near-field

enhancement [7, 11–13]. Photoelectrons provide an excellent window into understanding the dynamics of these interactions due to their sensitivity on the sub-wavelength spatial and ultrafast temporal scales. Photoelectron spectroscopy utilize these photoelectrons emitted during the interaction of a nanoparticle with an intense, femtosecond laser, allowing for the unraveling of the fundamental contributions to their acceleration, including enhanced near-fields, surface rescattering and charge interactions [14–16]. Experiments revealed the fundamental light-matter interaction processes during the optical response and associated electron dynamics in selected nanosystems, consistent with theoretical modeling of the induced plasmonic field near the nanostructure surface in the linear-response approximation [16–19].

However, recent investigations of nanoscale thin films and metasurfaces have revealed significant nonlinear (Kerr) effects [20, 21]. These motivate the study of such nonlinear effects in the optical response in composite nanostructures consisting of similar thin layers (e.g. core-shell nanoparticles).

Here, we investigate a type of core-shell nanoparticle specifically tailored to have a significant nonlinear effect which enables the intensity-dependent optical control of its plasmonic properties. This core-shell nanoparticle is comprised of a nanometer-thin gold coating encasing a larger dielectric silica core. We demonstrate, experimentally and theoretically, that as a function of the incident field intensity, a nonlinear response in the gold shell can

* These authors contributed equally to this work.

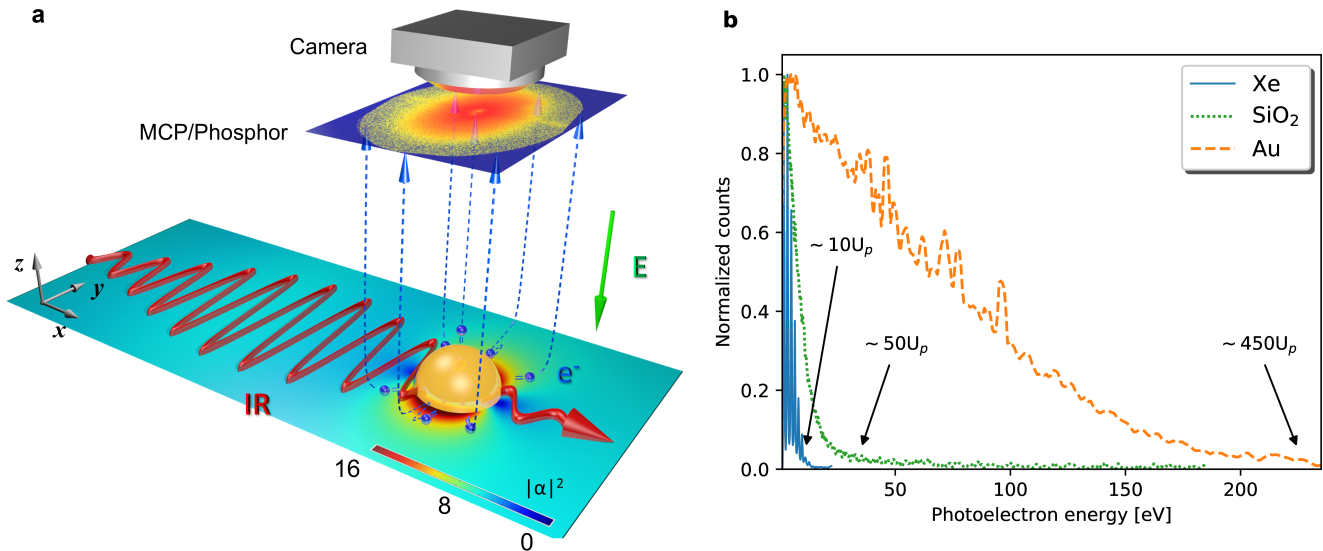


Figure 1. **Schematic of experiment and photoelectron spectra examples.** **a**, Schematic of an ultrafast laser interaction with a single, isolated nanoparticle in vacuum. The emitted photoelectrons are angle- and energy resolved using high-energy velocity map imaging (VMI) spectroscopy. **b**, Comparison of the obtained photoelectron energy distribution for photoemission from gaseous Xe (blue solid line), 120 nm diameter SiO₂ nanospheres (green dotted line), and 120 nm diameter Au nanospheres (gold dashed line), at a peak laser intensity of 8 TW/cm² at 780 nm wavelength. Respective cut-off energies in units of the ponderomotive energy U_p are indicated by arrows. All spectra are obtained from photoelectron counts within a 30° cone centered along the polarization direction.

71 be induced to control the plasmonic properties of the
 72 nanoparticle. At laser intensities below 0.1 TW/cm²,
 73 the linear response dominates, resulting in a large plasmonic
 74 near-field. However, with increasing intensity, the
 75 onset of a nonlinear component of the complex index of
 76 refraction for gold decreases the skin depth and effectively
 77 reduces the magnitude of the near-field. This ability
 78 to manipulate the plasmonic properties of core-shell
 79 nanoparticles solely by tuning the external-field intensity
 80 substantiates a new method of precise control over the
 81 optical response in layered nanomaterials.

82 RESULTS AND DISCUSSION

83 The photoelectron cut-off energy, defined as the high-
 84 est observable electron energy, has been established as a
 85 gold standard for probing the induced plasmonic near-
 86 fields close to various nanostructure surfaces of differ-
 87 ent materials [12, 13, 22, 23]. This cut-off scales linearly
 88 with the cycle-averaged quiver energy of a free electron
 89 in a laser field, referred to as the "ponderomotive en-
 90 ergy", $U_p = e^2 E^2 / 4m\omega^2 \propto I\lambda^2$ (e and m are electron
 91 charge and mass; E , I , ω , and λ designate the incident
 92 field strength, peak intensity, frequency, and wavelength
 93 of the laser pulse, respectively). Though near-fields are
 94 generally inhomogeneous (decreasing with distance), the
 95 fastest photoelectrons elastically rescatter and gain most

96 of their kinetic energies near the nanoparticle surface
 97 [16, 24], well within the typical spatial range of the
 98 near-field enhancement [7, 24, 25]. Therefore, rescaling
 99 photoelectron cut-off energies with the incident-field U_p
 100 reveals information about the plasmonic near-field en-
 101 hancements, independent of the incident-field intensity.

102 We determine the cut-off energies for single, isolated
 103 nanoparticles photoionized by femtosecond laser pulses,
 104 employing a high-energy velocity map imaging (VMI)
 105 spectrometer to measure the energy- and angle-resolved
 106 photoelectron spectra (see Methods for additional de-
 107 tails). Figure 1a illustrates a simplified schematic of
 108 the interaction and subsequent electron propagation and
 109 detection. Figure 1b shows the comparison of typical
 110 photoelectron energy spectra and their respective cut-
 111 off energies for atomic Xe, SiO₂ nanospheres, and Au
 112 nanospheres, exemplifying the substantial increase in the
 113 kinetic energy of electrons emitted from nanoparticles.

114 To demonstrate the feasibility of observing the signa-
 115 ture of the near-field in these nanosystems, we measured
 116 the size-dependent photoelectron cut-off energies for solid
 117 Au nanospheres. Figure 2a shows the cut-off energies for
 118 diameters ranging from 5 nm to 400 nm at several in-
 119 tensities. The plasmonic near-field response was inves-
 120 tigated by rescaling the cut-off energies to their respec-
 121 tive incident-field ponderomotive energy U_p , as shown in
 122 Fig. 2b. For comparison, the cut-off energies for SiO₂
 123 nanospheres at similar diameters and intensities are also

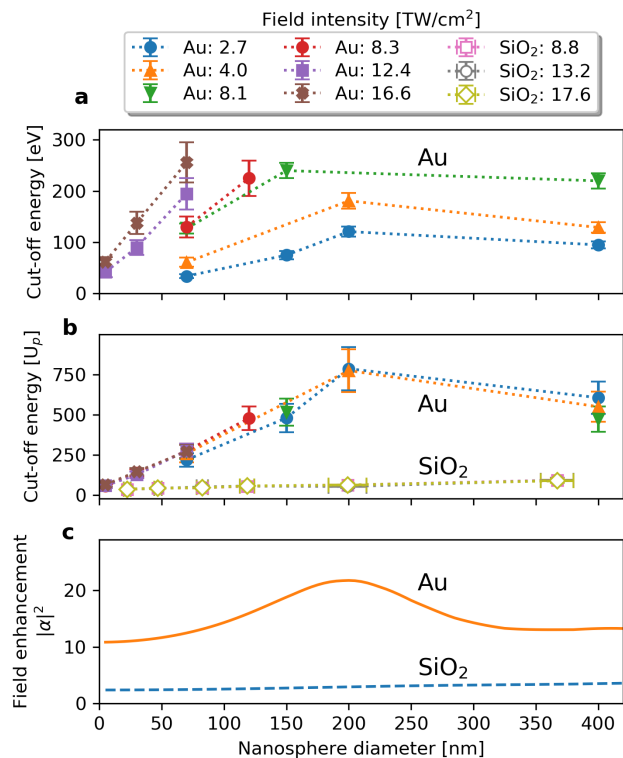


Figure 2. **Probing field enhancements with photoelectron cut-off energies.** **a**, Size-dependent maximum cut-off energies from experimental VMI spectra for various laser intensities for Au nanospheres in units of eV and for an incident pulse wavelength of 780 nm. **b**, The same cut-off energies as in **a** for Au and SiO₂ nanospheres rescaled to incident-field ponderomotive energy U_p . **c**, Simulated near-field enhancement $|\alpha|^2$ for Au (orange solid line) and SiO₂ nanospheres (blue dashed line).

124 plotted [15]. The U_p -rescaled cut-off energies for both
 125 materials are shown to be independent of the laser field
 126 intensity, within the size and intensity range of this work,
 127 as evidenced in Fig. 2b by the overlap of the data points
 128 for each particular size. The cut-off energies for Au
 129 nanospheres indicates a prominent peak at diameter $D =$
 130 200 nm and more energetic photoelectrons than for SiO₂
 131 nanoparticles, for which only a slight, monotonic increase
 132 with diameter occurs.

133 Further analysis in Fig. 2c reveals that the U_p -rescaled
 134 cut-off energies resemble the maximum near-field inten-
 135 sity enhancement (which we refer to as “field enhance-
 136 ment” $|\alpha|^2$), in Fig. 2b. For the results shown in Fig. 2c,
 137 we calculated the induced near-field by numerically solv-
 138 ing the Mie equations [26, 27] using indices of refrac-
 139 tion within the linear optical response for Au and SiO₂
 140 nanospheres [28]. The field enhancement is defined by
 141 the maximum total field intensity with respect to the in-
 142 cident intensity and typically located close to the particle
 143 surface [17, 18]. Though the exact dependence between

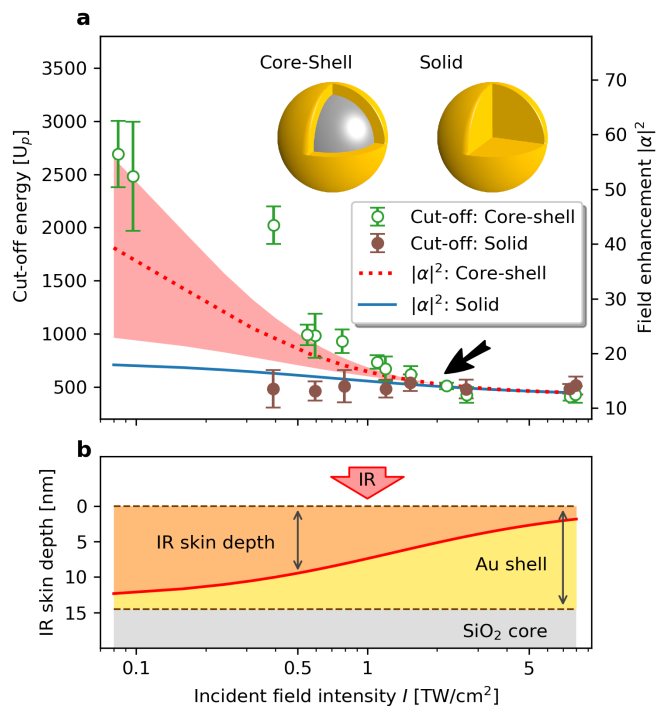


Figure 3. **Probing and analyzing intensity-dependent field enhancement of core-shell structures and solid Au nanospheres.** **a**, Maximum photoelectron cut-off energies in the units of incident-field ponderomotive energy U_p , for SiO₂-core-Au-shell structures (hollow markers) and solid Au nanospheres (solid markers), as a function of the incident-field intensity I . The core-shell structures have an outer diameter $D_2 = 147 \pm 7$ nm and an inner diameter $D_1 = 118 \pm 4$ nm, while the solid Au nanospheres have a diameter of 150 ± 5 nm. The simulated field enhancement $|\alpha|^2$ (scale on the right) for core-shell structures (red dotted line) and solid Au nanospheres (blue solid line) are also plotted for comparison. The red shaded area is the calculated uncertainty range caused by the manufacturing dispersity of the inner and outer radii of the core-shell structures (See Supplementary Note 4). The black arrow indicates the selected convergence of the core-shell and solid nanospheres in cut-off energies and in field enhancements. **b**, Calculated IR skin depth (red line and darkened area) for a Au shell thickness of 14.5 nm, as a function of the incident-field intensity I . All results are for an incident pulse wavelength of 780 nm.

144 the cut-off energy and field enhancement is determined by
 145 multiple effects (such as rescattering and Coulomb inter-
 146 actions) [14, 16], Fig. 2b and Fig. 2c reveal that the cut-
 147 off energy does, however, accurately reflect the dominant
 148 signature of field enhancement profiles for Au and SiO₂
 149 nanospheres (see Supplemental Note 2). This agreement
 150 supports our use of the cut-off energy as an indicator
 151 for observing changes in the magnitude of the plasmonic
 152 field enhancement.

153 To investigate the strong-field control of the plas-
 154 monic properties in a layered nanostructure, we examined
 155 SiO₂-core-Au-shell structures. Core-shell nanoparticles

were specifically chosen to elucidate any intensity-related changes to the field enhancement due to their unique configuration in comparison with solid Au nanospheres of a comparable size. The nanometer-thin Au shell surrounding a dielectric core results in a stronger localization of the plasmonic near-field when compared to solid Au nanospheres. We neglect any laser-induced propagation effects as the nanoparticle radius is much smaller than the incident pulse wavelength. Figure 3a shows our measured intensity-dependent photoelectron cut-off energies, rescaled with the incident-field ponderomotive energy U_p at 780 nm wavelength, for core-shell structures and solid Au nanospheres of approximately 150 nm diameter.

The U_p -rescaled cut-off energy for solid Au nanospheres remains approximately unchanged ($\sim 500 U_p$) for different incident-field intensities, indicating that the field enhancement near solid Au nanospheres is nearly independent of the intensity (Fig. 3a). In contrast, the cut-off energy for the core-shell structures varies drastically within the intensity range sampled. At low intensities, this energy is large when scaled by U_p ($2000 \sim 3000 U_p$, approximately 10 eV). However, it rapidly decreases and converges to the nearly identical value of the solid Au nanospheres beyond $\sim 2 \text{ TW/cm}^2$, as indicated by the black arrow in Fig. 3a. This implies that the field enhancement of the core-shell structure does not remain constant with the increasing laser intensity, but rather begins (at low intensity) at a value significantly higher for solid Au nanospheres, before quickly decreasing to a similar value at higher intensities. The contrast of these two particles is particularly strong at very low intensities ($\sim 0.1 \text{ TW/cm}^2$), where no photoemission is observed for solid Au nanospheres due to the extremely weak electromagnetic field. A measurable amount of photoelectrons with over $2000 U_p$ cut-off energy are still observed from core-shell structures, further confirming that a large field enhancement is induced at low intensities.

The nonlinear optical response of the Au shell is the key to understanding the observed effects in core-shell nanoparticles. Note that only the linear optical response is included in Fig. 2c. To introduce the nonlinear response, we apply a simple and widely used model to account for intensity-dependent changes in the index of refraction for Au [29],

$$n = n_0 + n_2 I, \quad (1)$$

where n_0 , an experimentally determined complex number [28], is the linear index of refraction employed for our simulation results in Fig. 2. n_2 is related to the third-order susceptibility $\chi^{(3)}$ (or Kerr effect) [30],

$$n_2 (\text{m}^2/\text{W}) = \frac{283}{n_0 \Re(n_0)} \chi^{(3)} (\text{m}^2/\text{V}^2). \quad (2)$$

$\Re(n_0)$ is the real part of n_0 and $\chi^{(3)} = (-9.1 + 0.35i) \times$

$10^{-19} \text{ m}^2/\text{V}^2$, according to a measurement using 15 nm Au films [31], close to the Au shell thickness in our work. At 780 nm wavelength, $n_2 = (0.026 + 3.65i) \times 10^{-12} (\text{W}/\text{cm}^2)^{-1}$ is predominantly imaginary. When $I \rightarrow 0$, the linear optical response dominates and $n \approx n_0$. As the intensity increases, the imaginary part $\Im(n) = \Im(n_0) + \Im(n_2) * I$ increases, and the nonlinear effect starts to emerge.

We estimate the normal-incident IR skin depth σ following [32] as,

$$\sigma = \frac{c}{2\omega \Im(n)} = \frac{c}{2\omega [\Im(n_0) + \Im(n_2) * I]}, \quad (3)$$

where c is the speed of light. Thus, the IR skin depth decreases with incident-field intensity in this particular situation. Figure 3b plots the intensity-dependent IR skin depth, in comparison with the Au shell thickness ($\sim 14.5 \text{ nm}$) of the core-shell structures. At low intensities ($< 0.1 \text{ TW/cm}^2$), the skin depth is approximately 13 nm, comparable to the Au shell thickness, suggesting a considerable amount of the IR field reaches the SiO_2 core. Since the optical response of a core-shell nanoparticle is extremely sensitive to the fields at both the inner and outer surfaces, their larger field enhancement results from the penetration of the external field into the Au- SiO_2 interface. This effect is incorporated by applying the boundary conditions at both interfaces when solving the Mie equations [7]. However, as the intensity increases, σ rapidly drops and approaches 2 nm at 8 TW/cm^2 , well below the Au-shell thickness, preventing the IR field from penetrating the Au shell, i.e., shielding the SiO_2 core. Therefore, the outer Au surface becomes the dominant factor for determining the optical response (and, thus, the field enhancement), causing the core-shell structures to appear to be indistinguishable from solid Au nanospheres of the same outer diameter.

Note that, while a recent study included the nonlinear response of SiO_2 nanoparticles [19], we neglect such effects in the SiO_2 core of the core-shell structures, since the field near the Au- SiO_2 interface is too heavily dampened (not exceeding 10^{10} W/cm^2) to induce any significant nonlinear response in this study.

Figure 3a also plots the Mie-simulated field enhancement $|\alpha|^2$ for core-shell structures and solid Au nanospheres, including the nonlinear optical response. The field enhancement of solid Au nanospheres only decreases slightly from 18 to 13 as the intensity increases. This indicates that the nonlinear response, while present in solid Au nanospheres, is insignificant and does not induce a measurable difference exceeding experimental uncertainty in this work, justifying our calculation of the results in Fig. 2 using a linear-response approximation. The core-shell structures, on the other hand, start with a field enhancement up to 60 at low intensities, where linear response dominates. This large enhancement is responsible for the photoemission observed from core-shell

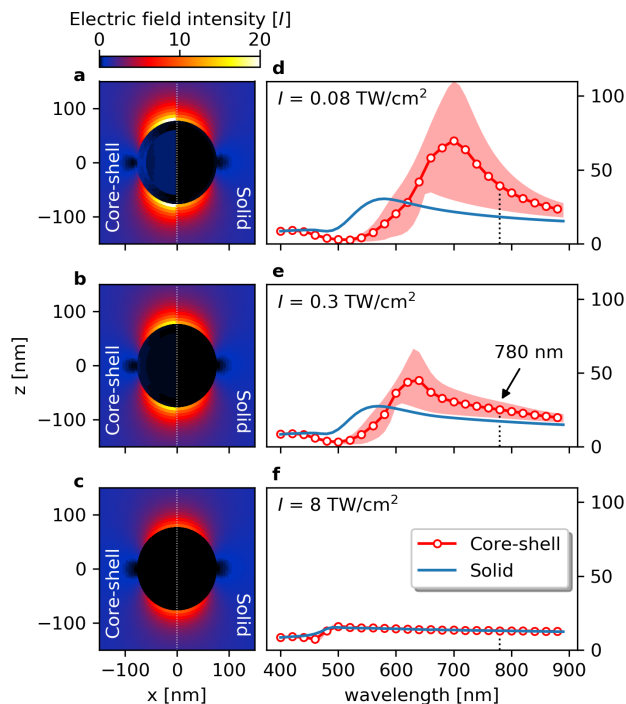


Figure 4. **Controlling plasmonic properties of core-shell structures.** **a-c**, Simulated inhomogeneous electric-field intensity distribution for core-shell structures (left half) and solid Au nanoparticles (right half), for the incident-field wavelength of 780 nm and intensities of (a) 0.08, (b) 0.3, and (c) 8 TW/cm². **d-f**, Simulated field enhancement $|\alpha|^2$ as a function of incident wavelength, under the same respective incident-field intensities, for core-shell (red circled lines) and solid Au nanoparticles (blue solid lines). The red shaded areas are the uncertainty range caused by the manufacturing dispersity of the inner and outer radii of the core-shell structures.

structures at low intensities, which is absent in solid Au nanoparticles, as well as the significantly larger cut-off energy. As the intensity increases, the nonlinear response results in a decreasing skin depth (Fig. 3b), leading to significantly smaller field enhancements that eventually converge with our results for the solid Au nanoparticles beyond ~ 2 TW/cm². The profiles of the simulated field enhancements, especially the convergence at ~ 2 TW/cm², are in excellent agreement with that of the measured cut-off energies for both nanoparticles. This success validates the use of the simple model in Eq. (1) and shows that the laser intensity has a significant impact on the plasmonic response of core-shell structures, in contrast to their solid Au counterparts.

A more in-depth understanding of such an impact and the broader implications can be achieved by extending our line of investigation to a larger spectral range. Figures 4d-f show the calculated field enhancement of core-shell structures and solid Au nanoparticles as a function of the incident-field wavelength for incident-field intensities

of 0.08, 0.3, and 8 TW/cm², respectively. For each corresponding incident-field intensity, Figs. 4a-c compare a section of our simulated electric-field-intensity distribution between the two types of nanoparticles for an incident field at 780 nm wavelength.

At 0.08 TW/cm², where the linear optical response dominates, a weak yet noticeable field penetrates the Au shell of the core-shell structure. The propagation of the external field across the Au-SiO₂ interface yields the significantly more intense and red-shifted resonant spectra, as compared with solid Au nanoparticles. Such pronounced differences show that the plasmonic response of core-shell structures, including the absorption resonance and the near-field magnitude, can be tuned by changing parameters in the production of the nanospheres (core diameter, shell thickness and composition) [7–10].

As the incident-field intensity increases, due to the growing nonlinear response of the Au shell preventing penetration of the field, the resonance feature for the core-shell structures starts to blue shift and decrease in magnitude, before gradually becoming indistinguishable to solid Au nanospheres across the spectra. We thus demonstrate that for core-shell nanoparticles, the tunable plasmonic response can be effectively switched “on” and “off” by simply controlling the external field intensity. For intensities well below a threshold (~ 2 TW/cm² in this work), the tunable plasmonic response of core-shell structures is switched “on”, manifesting a large and red-shifted resonance. For intensities above the threshold, the response is effectively switched “off”, and the core-shell structures appear to be indistinguishable from the solid Au nanospheres. According to Eq. (3), for a chosen material, such a threshold is determined primarily by the shell thickness, where a thinner shell requires a larger intensity threshold to ensure the IR skin depth is smaller than the shell thickness. This shows core-shell nanoparticles can be carefully synthesized to have a designated intensity threshold so that their plasmonic properties are controllable by manipulating the external field intensity.

CONCLUSIONS

We have demonstrated the ability to control the plasmonic response of a layered nanostructure solely by varying the laser intensity. This was accomplished by measuring the photoelectron cut-off energies from single, isolated core-shell nanoparticles and using them as a sensitive probe of the plasmonic field. Experimental signatures of a non-constant, intensity-dependent near-field were verified by a modified Mie theory as the direct result of the nonlinear optical response of the outer gold shell. Further analysis revealed that the decreasing skin depth into the nanoparticle surface at laser intensities above ~ 2 TW/cm² effectively shields the SiO₂ core, rendering the magnitude of its near-field identical to that of a solid

333 Au nanosphere. These results suggest a new intensity-
 334 dependent strong-field control of the plasmonic response
 335 in layered nanostructures. While such responses in lay-
 336 ered nanostructures are known to be tunable by their
 337 physical structure, we demonstrated that they can fur-
 338 ther be effectively switched “on” and “off” solely by con-
 339 trolling the external-field intensity.

340 This intensity-dependent optical control of the plas-
 341 monic response could hold the keys to new lines of re-
 342 search and implementations based on layered nanostruc-
 343 tures. For example, many applications require nanosys-
 344 tems such as core-shell structures to be tuned to precise
 345 resonant wavelengths [9, 10]. Our work unlocks a new
 346 tuning mechanism where a single core-shell structure can
 347 be manipulated to have an adjustable resonance and op-
 348 tical properties, dependent merely on the applied laser
 349 intensity. In other applications, such as photocatalysis
 350 [6] and field-induced molecular reactions [33], core-shell
 351 structures could be versatile substitutes for the currently
 352 used solid nanoparticles. Not only can they be tailored
 353 to provide larger field enhancements and substantially
 354 reduce the laser-intensity requirements, but such large
 355 enhancements can also be automatically turned “off” by
 356 the nonlinear response to avoid overexposure at high in-
 357 tensities. This can have significant impacts in areas such
 358 as metamaterials, plasmonics and opto-electronics.

359 [1] Stockman, M. I. Nanoplasmonics: The physics behind
 360 the applications. *Phys. Today* **64**, 39–44 (2011). URL
 361 [http://scitation.aip.org/content/aip/magazine/
 362 physicstoday/article/64/2/10.1063/1.3554315](http://scitation.aip.org/content/aip/magazine/physicstoday/article/64/2/10.1063/1.3554315).
 363 [2] Law, S., Yu, L., Rosenberg, A. & Wasserman, D. All-
 364 semiconductor plasmonic nanoantennas for infrared sens-
 365 ing. *Nano Letters* **13**, 4569–4574 (2013). URL <https://doi.org/10.1021/nl402766t>. PMID: 23987983.
 366 [3] Krausz, F. & Stockman, M. I. Attosecond metrology:
 367 from electron capture to future signal processing. *Nat.*
 368 *Photon.* **8**, 205–213 (2014). URL [https://doi.org/10.
 369 1038/nphoton.2014.28](https://doi.org/10.1038/nphoton.2014.28).
 370 [4] Sheldon, M. T., van de Groep, J., Brown, A. M.,
 371 Polman, A. & Atwater, H. A. Plasmoelectric po-
 372 tentials in metal nanostructures. *Science* **346**, 828–
 373 831 (2014). URL [http://science.sciencemag.org/
 374 content/346/6211/828](http://science.sciencemag.org/content/346/6211/828).
 375 [5] Zhang, X., Chen, Y. L., Liu, R.-S. & Tsai, D. P. Plas-
 376 monic photocatalysis. *Reports on Progress in Physics* **76**,
 377 046401 (2013).
 378 [6] Wu, T. *et al.* Surface plasmon resonance-induced vis-
 379 ible light photocatalytic reduction of graphene oxide:
 380 Using ag nanoparticles as a plasmonic photocatalyst.
 381 *Nanoscale* **3**, 2142–2144 (2011). URL [http://dx.doi.
 382 org/10.1039/C1NR10128E](http://dx.doi.org/10.1039/C1NR10128E).
 383 [7] Li, J., Saydanzad, E. & Thumm, U. Imaging Plasmonic
 384 Fields with Atomic Spatiotemporal Resolution. *Phys.*
 385 *Rev. Lett.* **120**, 223903 (2018). URL [https://link.aps.
 386 org/doi/10.1103/PhysRevLett.120.223903](https://link.aps.org/doi/10.1103/PhysRevLett.120.223903).
 387 [8] Hirsch, L. R. *et al.* Metal nanoshells. *Annals of Biomed-*
 388

ical Engineering **34**, 15–22 (2006). URL [https://doi.
 389 org/10.1007/s10439-005-9001-8](https://doi.org/10.1007/s10439-005-9001-8).
 390 [9] Rastinehad, A. R. *et al.* Gold nanoshell-localized pho-
 391 tothermal ablation of prostate tumors in a clinical pi-
 392 lot device study. *Proceedings of the National Academy
 393 of Sciences* **116**, 18590–18596 (2019). URL <https://www.pnas.org/content/116/37/18590>.
 394 [10] Chen, W. *et al.* Targeting of Pancreatic Cancer
 395 with Magneto-Fluorescent Theranostic Gold Nanoshells.
 396 *Nanomedicine* **9**, 1209–1222 (2014). URL [https://dx.
 397 doi.org/10.2217/2Fnm.13.84](https://dx.doi.org/10.2217/2Fnm.13.84).
 398 [11] Li, J. *Spatiotemporally resolved photoemission from plas-*
 399 *monic nanoparticle*. Ph.D. thesis, Kansas State Univer-
 400 sity (2020). URL [https://krex.k-state.edu/dspace/
 401 handle/2097/40310](https://krex.k-state.edu/dspace/handle/2097/40310).
 402 [12] Thomas, S., Krüger, M., Förster, M., Schenk, M. &
 403 Hommelhoff, P. Probing of optical near-fields by elec-
 404 tron rescattering on the 1 nm scale. *Nano Letters*
 405 **13**, 4790–4794 (2013). URL [https://doi.org/10.1021/
 406 nl402407r](https://doi.org/10.1021/nl402407r). PMID: 24032432.
 407 [13] Rácz, P. *et al.* Measurement of nanoplasmonic field en-
 408 hancement with ultrafast photoemission. *Nano Letters*
 409 **17**, 1181–1186 (2017). URL [https://doi.org/10.1021/
 410 acs.nanolett.6b04893](https://doi.org/10.1021/acs.nanolett.6b04893). PMID: 28094992.
 411 [14] Süßmann, F. *et al.* Field propagation-induced direc-
 412 tionality of carrier-envelope phase-controlled photoemis-
 413 sion from nanospheres. *Nature Communications* **6**, 7944
 414 (2015). URL <https://doi.org/10.1038/ncomms8944>.
 415 [15] Powell, J. A. *et al.* Interplay of pulse duration, peak
 416 intensity, and particle size in laser-driven electron emis-
 417 sion from silica nanospheres. *Opt. Express* **27**, 27124–
 418 27135 (2019). URL [http://www.opticsexpress.org/
 419 abstract.cfm?URI=oe-27-19-27124](http://www.opticsexpress.org/abstract.cfm?URI=oe-27-19-27124).
 420 [16] Zherebtsov, S. *et al.* Controlled near-field enhanced elec-
 421 tron acceleration from dielectric nanospheres with intense
 422 few-cycle laser fields. *Nature Physics* **7**, 656–662 (2011).
 423 URL <https://doi.org/10.1038/nphys1983>.
 424 [17] Li, J., Saydanzad, E. & Thumm, U. Retrieving
 425 plasmonic near-field information: A quantum-
 426 mechanical model for streaking photoelectron spec-
 427 troscopy of gold nanospheres. *Phys. Rev. A* **94**,
 428 051401 (2016). URL [http://link.aps.org/doi/10.
 429 1103/PhysRevA.94.051401](http://link.aps.org/doi/10.1103/PhysRevA.94.051401).
 430 [18] Li, J., Saydanzad, E. & Thumm, U. Attosecond
 431 time-resolved streaked photoelectron spectroscopy of
 432 transition-metal nanospheres. *Phys. Rev. A* **95**, 043423
 433 (2017). URL [https://link.aps.org/doi/10.1103/
 434 PhysRevA.95.043423](https://link.aps.org/doi/10.1103/PhysRevA.95.043423).
 435 [19] Rupp, P. *et al.* Few-cycle laser driven reaction nanoscopy
 436 on aerosolized silica nanoparticles. *Nature Communica-*
 437 *tions* **10**, 4655 (2019). URL [https://doi.org/10.1038/
 438 s41467-019-12580-0](https://doi.org/10.1038/s41467-019-12580-0).
 439 [20] Xiao, Y., Qian, H. & Liu, Z. Nonlinear metasurface based
 440 on giant optical kerr response of gold quantum wells. *ACS*
 441 *Photonics* **5**, 1654–1659 (2018). URL [https://doi.org/
 442 10.1021/acsp Photonics.7b01140](https://doi.org/10.1021/acsp Photonics.7b01140).
 443 [21] Nookala, N. *et al.* Ultrathin gradient nonlinear metasur-
 444 face with a giant nonlinear response. *Optica* **3**, 283–288
 445 (2016). URL [http://www.osapublishing.org/optica/
 446 abstract.cfm?URI=optica-3-3-283](http://www.osapublishing.org/optica/abstract.cfm?URI=optica-3-3-283).
 447 [22] Wang, Z. *et al.* Universal high-energy photoelectron
 448 emission from nanoclusters beyond the atomic limit.
 449 *Phys. Rev. Lett.* **124**, 173201 (2020). URL [https://
 450 link.aps.org/doi/10.1103/PhysRevLett.124.173201](https://link.aps.org/doi/10.1103/PhysRevLett.124.173201).
 451
 452

- 453 [23] Schötz, J. *et al.* Onset of space-charge effects in strong-
454 field photocurrents from nanometric needle tips (2021).
455 2106.00503.
- 456 [24] Summers, A. M. *Strong-field interactions in atoms and*
457 *nanosystems: advances in fundamental science and tech-*
458 *nological capabilities of ultrafast sources.* Ph.D. thesis,
459 Kansas State University (2019). URL [https://krex.](https://krex.k-state.edu/dspace/handle/2097/39413)
460 [k-state.edu/dspace/handle/2097/39413](https://krex.k-state.edu/dspace/handle/2097/39413).
- 461 [25] Süßmann, F. & Kling, M. F. Attosecond nanoplasmonic
462 streaking of localized fields near metal nanospheres.
463 *Phys. Rev. B* **84**, 121406 (2011). URL [http://link.](http://link.aps.org/doi/10.1103/PhysRevB.84.121406)
464 [aps.org/doi/10.1103/PhysRevB.84.121406](http://link.aps.org/doi/10.1103/PhysRevB.84.121406).
- 465 [26] Mie, G. Beiträge zur Optik trüber Medien, speziell kol-
466 loidaler Metallösungen. *Annalen der Physik* **330**, 377–
467 445 (1908). URL [http://dx.doi.org/10.1002/andp.](http://dx.doi.org/10.1002/andp.19083300302)
468 [19083300302](http://dx.doi.org/10.1002/andp.19083300302).
- 469 [27] Stratton, J. *Electromagnetic theory*, vol. 33 (Wi-
470 ley, 2007). URL [http://books.google.com/books?](http://books.google.com/books?hl=en&lr=&id=zFeWdS2luE4C&oi=fnd&pg=PA1&dq=electromagnetic+theory+stratton&ots=8T5nXodjoo&sig=cv6oK09UF6g8BZkPvqjCesJjSs8)
471 [hl=en&lr=&id=zFeWdS2luE4C&oi=fnd&pg=PA1&dq=](http://books.google.com/books?hl=en&lr=&id=zFeWdS2luE4C&oi=fnd&pg=PA1&dq=electromagnetic+theory+stratton&ots=8T5nXodjoo&sig=cv6oK09UF6g8BZkPvqjCesJjSs8)
472 [electromagnetic+theory+stratton&ots=8T5nXodjoo&](http://books.google.com/books?hl=en&lr=&id=zFeWdS2luE4C&oi=fnd&pg=PA1&dq=electromagnetic+theory+stratton&ots=8T5nXodjoo&sig=cv6oK09UF6g8BZkPvqjCesJjSs8)
473 [sig=cv6oK09UF6g8BZkPvqjCesJjSs8](http://books.google.com/books?hl=en&lr=&id=zFeWdS2luE4C&oi=fnd&pg=PA1&dq=electromagnetic+theory+stratton&ots=8T5nXodjoo&sig=cv6oK09UF6g8BZkPvqjCesJjSs8).
- 474 [28] Johnson, P. B. & Christy, R. W. Optical Con-
475 stants of the Noble Metals. *Phys. Rev. B* **6**, 4370–
476 4379 (1972). URL [https://link.aps.org/doi/10.](https://link.aps.org/doi/10.1103/PhysRevB.6.4370)
477 [1103/PhysRevB.6.4370](https://link.aps.org/doi/10.1103/PhysRevB.6.4370).
- 478 [29] Boyd, R. W. *Nonlinear optics* (Academic Press, 2008).
- 479 [30] Boyd, R. W., Shi, Z. & Leon, I. D. The third-
480 order nonlinear optical susceptibility of gold. *Op-*
481 *tics Communications* **326**, 74–79 (2014). URL
482 [http://www.sciencedirect.com/science/article/](http://www.sciencedirect.com/science/article/pii/S0030401814002351)
483 [pii/S0030401814002351](http://www.sciencedirect.com/science/article/pii/S0030401814002351).
- 484 [31] Qian, H., Xiao, Y. & Liu, Z. Giant kerr response of
485 ultrathin gold films from quantum size effect. *Nature*
486 *Communications* **7**, 13153 (2016). URL [https://doi.](https://doi.org/10.1038/ncomms13153)
487 [org/10.1038/ncomms13153](https://doi.org/10.1038/ncomms13153).
- 488 [32] Hecht, E. *Optics* (Reading, Mass. : Addison-Wesley,
489 Reading, Mass., 2002), 4th edition.. edn.
- 490 [33] Rosenberger, P. *et al.* Near-field induced reaction yields
491 from nanoparticle clusters. *ACS Photonics* **7**, 1885–1892
492 (2020). URL [https://doi.org/10.1021/acsp Photonics.](https://doi.org/10.1021/acsp Photonics.0c00823)
493 [0c00823](https://doi.org/10.1021/acsp Photonics.0c00823).
- 494 [34] Kling, N. G. *et al.* Thick-lens velocity-map imaging spec-
495 trometer with high resolution for high-energy charged
496 particles. *Journal of Instrumentation* **9**, P05005–P05005
497 (2014). URL [https://doi.org/10.1088%2F1748-0221%](https://doi.org/10.1088%2F1748-0221%2F9%2F05%2Fp05005)
498 [2F9%2F05%2Fp05005](https://doi.org/10.1088%2F1748-0221%2F9%2F05%2Fp05005).
- 499 [35] Powell, J. *Strong-field driven dynamics of metal and di-*
500 *electric nanoparticles.* Ph.D. thesis, Kansas State Uni-
501 versity (2017).
- 502 [36] Palik, E. *Handbook of Optical Constants of Solids* (El-
503 sevier Science, 1985). URL [http://books.google.com/](http://books.google.com/books?id=h8mEd9no5-kC)
504 [books?id=h8mEd9no5-kC](http://books.google.com/books?id=h8mEd9no5-kC).
- 511 amplification (CPA) system generating 25 fs pulses at
512 780 nm central wavelength. Photoelectron spectra were
513 captured in a thick-lens, high-energy velocity map imag-
514 ing (VMI) spectrometer [34] capable of gathering up to
515 350 eV electron energy. The custom nanoparticle source
516 produces a continuous beam of nanoparticles into vac-
517 uum. Spherical nanoparticle samples were selected for
518 their narrow size distribution and overall purity. The
519 initial nanoparticle concentration was also carefully cho-
520 sen to avoid the formation of clusters in the nanoparticle
521 beam.

522 Laser intensity characterization

523 The peak laser intensity was determined by analyzing
524 the above-threshold (ATI) photoelectron energy distri-
525 bution of atomic Xe with the aforementioned VMI un-
526 der similar experimental parameters. The ponderomotive
527 shift of the Xe ATI comb was measured as a function of
528 the input-laser pulse energy, in order to derive the pon-
529 deromotive energy, $U_p \propto I\lambda^2$, and thus, the peak laser
530 intensity I [24, 35]. For intensities below the ionization
531 threshold of Xe, the ratio of the pulse energies was used
532 to extrapolate the peak intensity. See Supplementary
533 Note 1 for more detail.

534 Photoelectron cut-off determination

535 The nanoparticle photoelectron cut-off energy was ex-
536 tracted from the experimental VMI images in a method
537 described in previous work [15, 35]. The detected elas-
538 tically back-scattered photoelectrons are obtained from
539 the non-inverted VMI images, for which the upper energy
540 boundaries of the full 3D momentum sphere and the 2D
541 projection are essentially the same. A radial distribution
542 of these projections along the polarization direction ac-
543 curately determines the maximum photoelectron energy.

544 Mie simulations

545 We simulated laser-induced plasmonic near-fields by
546 solving the Mie equations [26, 27] for plane waves scat-
547 tered by spherical objects. The linear terms of the di-
548 electric response of Au and SiO₂ enters as the frequency-
549 dependent complex-valued index of refraction obtained
550 from experiments [28, 36]. Our inclusion of nonlinear
551 effects is discussed in the text. The original Mie equa-
552 tions apply only to the solid spheres. For the simulations
553 of core-shell structures, we extended the traditional Mie
554 theory as outlined in Supplementary Note 3.

505 METHODS

506 Experimental setup

507 The laser setup and electron detection apparatus at
508 the James R. Macdonald Laboratory at Kansas State
509 University are described in more detail in [15]. Briefly,
510 the experiments used a Ti:Sapphire-based chirped pulse

ACKNOWLEDGMENT

555 This work was supported by the Air Force Office of Sci-
557 entific Research under award number FA9550-17-1-0369.
558 J.L., E.S. and U.T. acknowledge the support by the NSF
559 Grant No. 1802085. A.S. and D.R. were supported by
560 the Chemical Sciences, Geosciences, and Biosciences Di-
561 vision, Office of Basic Energy Sciences, Office of Science,
562 U. S. Department of Energy under Award No. DEFG02-
563 86ER13491, which also covered laser operational costs.
564 M.F.K acknowledges support by the German Research
565 Foundation (DFG) via SPP1840, and by the European
566 Research Council (ERC) via the FETopen project Peta-
567 COM.

AUTHOR CONTRIBUTIONS

569 J.P. and J.L. contributed equally to this work. J.P.,
570 J.L., A.S., U.T. and A.R. conceptualized and conducted
571 the study. J.P., A.S., S.J.R, M.D. and P.R. contributed
572 to performing the experiment. J.P. and A.S. performed
573 the data analysis. J.L. and U.T. developed the theo-
574 retical model, performed the simulations and interpreted
575 the results. J.P., J.L., A.S., E.S., C.M.S., D.R., M.F.K.,
576 C.T.H., U.T. and A.R. discussed the results. J.L., J.P.
577 and A.S. wrote the initial manuscript, which was revised
578 with input from all authors.

ADDITIONAL INFORMATION

580 The authors declare no competing financial interests.

Supplementary Information

Jeffrey Powell,^{1,2,3,*} Jianxiong Li,^{1,4,*} Adam Summers,^{1,5} Seyyed Javad Robotjazi,¹

Michael Davino,² Philipp Rupp,⁶ Erfan Saydanzad,¹ Christopher M. Sorensen,¹ Daniel

Rolles,¹ Matthias F. Kling,^{6,7} Carlos Trallero-Herrero,^{1,2} Uwe Thumm,¹ and Artem Rudenko¹

¹*J. R. Macdonald Laboratory, Department of Physics,*

Kansas State University, Manhattan, Kansas 66506, USA

²*Department of Physics, University of Connecticut, Storrs, Connecticut 06269, USA*

³*INRS, Énergie, Matériaux et Télécommunications,*

1650 Bld. Lionel Boulet, Varennes, Québec, J3X1S2, Canada

⁴*Department of Physics and Astronomy, Louisiana State University, Baton Rouge, Louisiana 70803, USA*

⁵*ICFO - Institut de Ciències Fòniques, The Barcelona Institute*

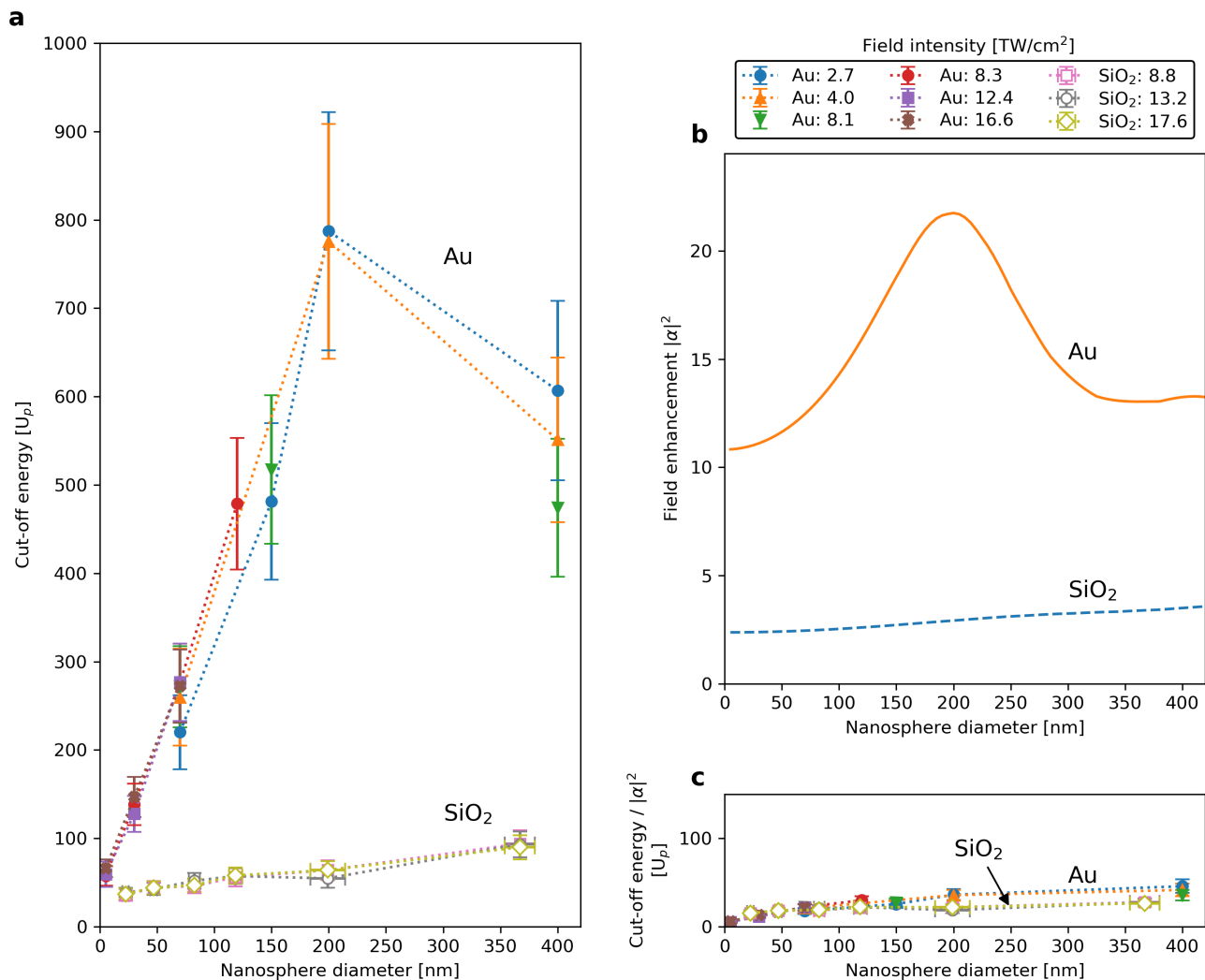
of Science and Technology, 08860 Castelldefels (Barcelona), Spain

⁶*Physics Department, Ludwig-Maximilians-Universität Munich, D-85748 Garching, Germany*

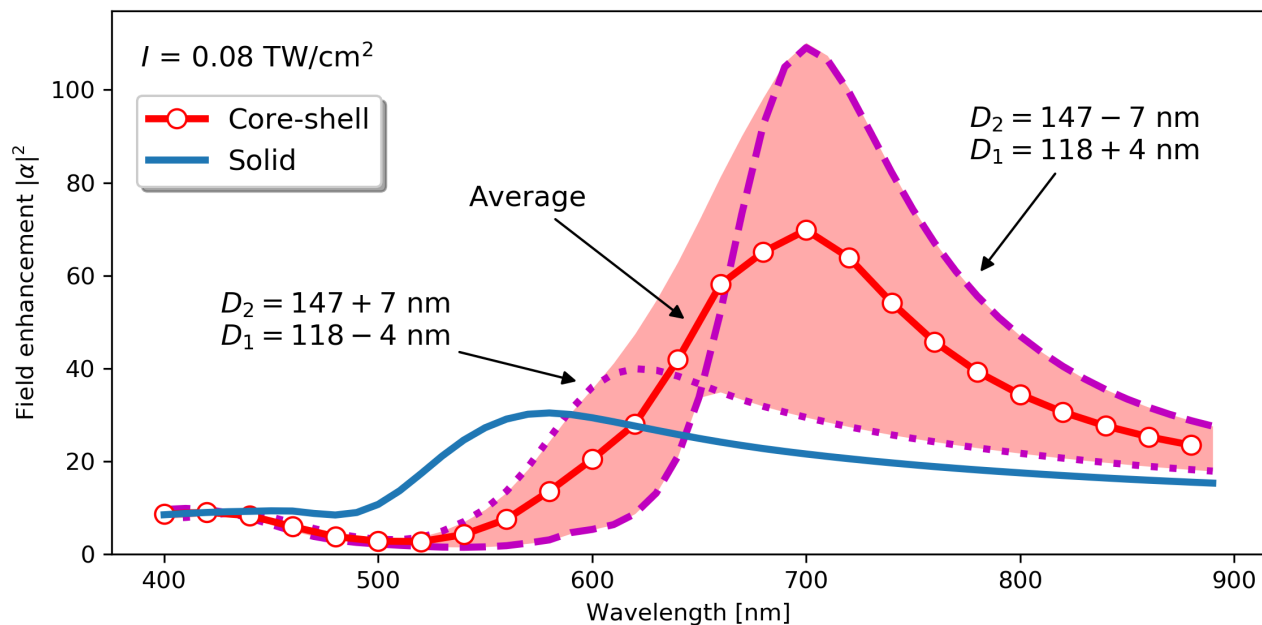
⁷*Max Planck Institute of Quantum Optics, D-85748 Garching, Germany*

(Dated: August 17, 2021)

* These authors contributed equally to this work.



Supplementary Figure S1. **a**, Size-dependent cut-off energies (re-scaled to the incident-field ponderomotive energy U_p) from experimental VMI spectra for Au and SiO₂ nanospheres, various laser intensities, and a laser wavelength $\lambda = 780$ nm. **b**, The Mie-simulated field enhancement $|\alpha|^2$ for Au (orange solid line) and SiO₂ nanospheres (blue dashed line). **c**, The same cut-off energies as in **a** for Au and SiO₂ nanospheres, shown on the same scale as in **a**, but divided by $|\alpha|^2$ to exclude the contribution from field enhancement.



Supplementary Figure S2. Illustration of the field-enhancement uncertainty as a result of manufacturing size dispersity (re-plot of Fig. ??d). The core-shell structure has an outer diameter of $D_2 = 147 \pm 7 \text{ nm}$ and an inner diameter of $D_1 = 118 \pm 4 \text{ nm}$. The purple dashed line is the field enhancement $|\alpha|^2$ simulated for $D_2 = 147 - 7 \text{ nm}$ and $D_1 = 118 + 4 \text{ nm}$ (thinnest shell). The purple dotted line is simulated for $D_2 = 147 + 7 \text{ nm}$ and $D_1 = 118 - 4 \text{ nm}$ (thickest shell). The red shaded area is the uncertainty range simulated with all possible combinations of outer and inner radii within the manufacturing dispersity. The red circled line is the average value within such uncertainty at each wavelength. The field enhancement of the solid Au nanoparticles of the same size is shown for comparison as the blue solid line. The intensity of the simulation is $I = 0.08 \text{ TW/cm}^2$.

SUPPLEMENTARY NOTE 1: EXPERIMENTAL SETUP

The experimental setup for imaging and measuring photoelectron emission made use of a thick-lens, high-energy velocity map imaging (VMI) spectrometer as described in [1]. Laser pulses with a central wavelength of $\lambda = 780$ nm and pulse duration of 25 fs were focused into the nanoparticle beam at the center of the interaction region of the VMI spectrometer. The intensity of the laser field was adjusted by a $\lambda/2$ waveplate in combination with a linear polarizer while the polarization was in the plane of the detector. The emitted electrons were projected onto a paired microchannel plate (MCP) and phosphor screen (P47 type), and the resulting images were recorded by a CMOS camera (Mikrotron EoSens 3CXP). The MCP was gated (200 - 400 ns) on the arrival time of the electrons using a high-voltage switch which effectively reduced the background contribution. The use of a real-time hit-finder software routine allowed for single-shot photoelectron spectra to be collected at greater than 1 kHz. The nanoparticle spectra were then analyzed by taking a radial projection along the polarization direction to determine the photoelectron cut-off.

The nanoparticle source delivers a continuous beam of single, isolated nanoparticles to the interaction volume in the direction perpendicular to the laser propagation. The source aerosolizes a colloid of nanoparticles that are subsequently dried by a solid-state counter-flow membrane dryer to remove the solvent (water) from the carrier gas (N_2). Additional care was taken to minimize the probability of clusters in the nanoparticle beam to prevent an amalgamation of photoelectrons from monomers and clusters [2] by keeping the number density below 10^{10} nanoparticles per mL. The in-vacuum beam density was increased using an aerodynamic lens system to focus the gas-phase nanoparticles while a three-stage differentially pumped arrangement removed excess carrier gas in vacuum. The typical pressure in the experimental chamber was 10^{-6} Torr with the nanoparticle source running, while the background pressure was 10^{-8} Torr.

Spherical nanoparticle samples were selected for their narrow size distribution ($<12\%$), solvent choice and overall purity from commercially available sources. Solid gold nanoparticles (Cytodiagnostics, Inc) were stabilized with citrate while gold nanoshells and SiO_2 nanospheres (nanoComposix, Inc) were coated with polyethylene glycol (PEG, 5kDa) and silanol, respectively.

To measure the laser intensity and calibrate the VMI, above-threshold ionization (ATI) in Xe was measured at the same laser parameters as for the nanoparticles. The ponderomotive shift of the Xe ATI comb was measured as a

function of the input laser pulse energy in order to derive the ponderomotive energy, $U_p = e^2 E^2 / 4m\omega^2 \propto I\lambda^2$, and thus, the peak laser intensity I . For experimental intensities below the ionization threshold of Xe, the ratio of the pulse energies was used to extrapolate the peak intensity. The spacing of consecutive Xe ATI peaks corresponds to the central incident photon energy and was used for energy calibration of the VMI [1].

SUPPLEMENTARY NOTE 2: FURTHER DISCUSSION ABOUT THE RELATION BETWEEN CUT-OFF ENERGY AND FIELD ENHANCEMENT

Figure ?? in the main text illustrates the relation between U_p -scaled cut-off energies and simulated field enhancements. It supports our use of the cut-off energy as an indicator for observing changes in field enhancement. A more detailed illustration can be seen in Fig. S1.

Figures S1a-b are plotted with the same data set as in Figs. ??b-c in the main text, respectively. Figure S1c shows the same cut-off energies as Fig. ??a, but divided by $|\alpha|^2$, to scale out the contribution from field enhancement. Both Fig. S1a and Fig. S1c are plotted on the same vertical scale as a comparison.

By scaling out the field enhancement contribution, Fig. S1c shows much lower and nearly flat curves for both Au and SiO₂ nanospheres, as compared to Fig. S1a. In addition, the differences between two materials are significantly reduced. Even though previous research showed that the exact dependence between the cut-off energy and field enhancement is convoluted due to multiple contributing factors [3, 4], Fig. S1c shows that field enhancement is the main contributor governing the changes in cut-off energies, within the range of our experimental parameters. This allows us to use the cut-off energy as an indicator for changes in the field enhancement.

It is also worth mentioning that this relation is seemingly less accurate for small nanoparticles by comparing Fig. S1a and Fig. S1b. However, Fig. S1c still shows good convergence at small sizes due to the fact that the photoelectron yield decreases as the nanoparticles size decreases [4]. Since electron-electron interaction is reportedly a significant component in the photoelectron dynamics [4], a decreasing photoelectron yield causes a decrease in the overall electron-electron interaction and, ultimately, the cut-off energies for both small Au and SiO₂ nanospheres, reducing the difference in U_p by directly comparing Fig. ??a and Fig. ??b.

We compared the core-shell structures and solid Au nanospheres of the same outer diameter (~ 150 nm). Therefore, the observed differences in cut-off energies are mainly due to the differences in the field enhancements.

SUPPLEMENTARY NOTE 3: MODIFIED MIE EQUATIONS FOR CORE-SHELL STRUCTURES

Mie theory is a well established theory to simulate the electromagnetic fields of plane waves scattered by spherical objects [5, 6]. The original Mie theory is restricted to solid spherical objects with a single spatially homogeneous index of refraction. This theory is sufficient to simulate the near fields of solid Au and SiO₂ nanospheres, as produced in Fig. ?? in the main text. Simulating the scattering fields for core-shell structures, however, requires its extension. Taking advantage of the spherical symmetry, these modifications can be included analytically as follows.

Suppose an incident plane wave with frequency ω travels in vacuum (index of refraction $n_0 = 1$) along the positive $\hat{\mathbf{z}}$ -axis, with the electric component polarized along the $\hat{\mathbf{x}}$ -axis. Its electric field is given by,

$$\mathbf{E}_i(\mathbf{r}, t) = \hat{\mathbf{x}}E_0e^{ik_0z-i\omega t}, \quad (\text{S1})$$

where E_0 is the incident-field amplitude, the subscript “0” stands for vacuum, and “*i*” stands for “*incident*”. We consider a spherical core-shell nanoparticle centered at the origin of our coordinate system, with inner and outer radii $R_1 = D_1/2$ and $R_2 = D_2/2$, respectively. The core and shell materials are assumed to have homogeneous, complex-valued indices of refraction of n_1 and n_2 , respectively. For convenience, we neglect magnetic materials in this discussion, and set permeability of all materials to 1.

The total electro-magnetic field can now be expressed as,

$$\mathbf{E}(\mathbf{r}, t) = \begin{cases} \mathbf{E}_i(\mathbf{r}, t) + \mathbf{E}_r(\mathbf{r}, t) \\ \mathbf{E}_s(\mathbf{r}, t) \\ \mathbf{E}_t(\mathbf{r}, t) \end{cases}, \quad \mathbf{H}(\mathbf{r}, t) = \begin{cases} \mathbf{H}_i(\mathbf{r}, t) + \mathbf{H}_r(\mathbf{r}, t) & (r > R_2) \\ \mathbf{H}_s(\mathbf{r}, t) & (R_1 < r < R_2) \\ \mathbf{H}_t(\mathbf{r}, t) & (0 < r < R_1) \end{cases}, \quad (\text{S2})$$

where the subscript/superscript r, s, t stand for “*reflected*”, “*shell*”, and “*transmitted*”, respectively.

Following Stratton [6], the incident plane wave can be written as,

$$\mathbf{E}_i(\mathbf{r}, t) = \hat{\mathbf{x}}E_0e^{ik_0z-i\omega t} = E_0e^{-i\omega t} \sum_{n=1}^{\infty} i^n \frac{2n+1}{n(n+1)} \left[\mathbf{m}_{o1n}^{(1)}(k_0\mathbf{r}) - i\mathbf{n}_{e1n}^{(1)}(k_0\mathbf{r}) \right] \quad (\text{S3a})$$

$$\mathbf{H}_i(\mathbf{r}, t) = \hat{\mathbf{y}} \frac{k_0}{\omega} E_0 e^{ik_0z-i\omega t} = -\frac{k_0 E_0}{\omega} e^{-i\omega t} \sum_{n=1}^{\infty} i^n \frac{2n+1}{n(n+1)} \left[\mathbf{m}_{e1n}^{(1)}(k_0\mathbf{r}) + i\mathbf{n}_{o1n}^{(1)}(k_0\mathbf{r}) \right], \quad (\text{S3b})$$

where $k_0 = 2\pi/\lambda = \omega/c$ is the wave vector. The two special functions are defined in spherical coordinates as,

$$\mathbf{m}_{\varepsilon mn}^{(q)}(\mathbf{kr}) = \pm \hat{\theta} \frac{m}{\sin \theta} z_n^{(q)}(kr) P_n^m(\cos \theta) \frac{\cos m\phi - \hat{\phi} z_n^{(q)}(kr) \frac{\partial P_n^m(\cos \theta)}{\partial \theta}}{\sin m\phi} \sin m\phi \quad (\text{S4a})$$

$$\begin{aligned} \mathbf{n}_{\varepsilon mn}^{(q)}(\mathbf{kr}) &= \hat{\mathbf{r}} \frac{n(n+1)}{kr} z_n^{(q)}(kr) P_n^m(\cos \theta) \frac{\sin m\phi + \hat{\theta} \frac{1}{kr} [kr z_n^{(q)}(kr)]'}{\cos m\phi} \frac{\partial P_n^m(\cos \theta)}{\partial \theta} \sin m\phi \\ &\pm \hat{\phi} \frac{m}{kr \sin \theta} [kr z_n^{(q)}(kr)]' P_n^m(\cos \theta) \frac{\cos m\phi}{\sin m\phi} , \end{aligned} \quad (\text{S4b})$$

where the superscripts $q = (1, 2, 3, 4)$ refer to the four spherical Bessel and Hankel functions $(j_n, y_n, h_n^{(1)}, h_n^{(2)})$ that replace $z_n^{(q)}$, respectively, and the prime denotes differentiation with respect to the argument kr . Since the incident field contains only $m = 1$ terms, all $m \neq 1$ terms are trivial in our derivation.

As within the original Mie theory [5, 6], the field in vacuum, *i.e.*, outside of the core-shell structure (“reflected” field), can be written as,

$$\mathbf{E}_r(\mathbf{r}, t) = E_0 e^{-i\omega t} \sum_{n=1}^{\infty} i^n \frac{2n+1}{n(n+1)} \left[a_n^r \mathbf{m}_{o1n}^{(3)}(k_0 \mathbf{r}) - i b_n^r \mathbf{n}_{e1n}^{(3)}(k_0 \mathbf{r}) \right] \quad (\text{S5a})$$

$$\mathbf{H}_r(\mathbf{r}, t) = -\frac{k_0 E_0}{\omega} e^{-i\omega t} \sum_{n=1}^{\infty} i^n \frac{2n+1}{n(n+1)} \left[b_n^r \mathbf{m}_{e1n}^{(3)}(k_0 \mathbf{r}) + i a_n^r \mathbf{n}_{o1n}^{(3)}(k_0 \mathbf{r}) \right], \quad (\text{S5b})$$

with undetermined coefficients (a_n^r, b_n^r) . The spherical Hankel functions of the first kind ($q = 3$) are chosen for outgoing waves. The field inside the core (“transmitted” field) can be written as,

$$\mathbf{E}_t(\mathbf{r}, t) = E_0 e^{-i\omega t} \sum_{n=1}^{\infty} i^n \frac{2n+1}{n(n+1)} \left[a_n^t \mathbf{m}_{o1n}^{(1)}(k_1 \mathbf{r}) - i b_n^t \mathbf{n}_{e1n}^{(1)}(k_1 \mathbf{r}) \right] \quad (\text{S6a})$$

$$\mathbf{H}_t(\mathbf{r}, t) = -\frac{k_1 E_0}{\omega} e^{-i\omega t} \sum_{n=1}^{\infty} i^n \frac{2n+1}{n(n+1)} \left[b_n^t \mathbf{m}_{e1n}^{(1)}(k_1 \mathbf{r}) + i a_n^t \mathbf{n}_{o1n}^{(1)}(k_1 \mathbf{r}) \right], \quad (\text{S6b})$$

with undetermined coefficients (a_n^t, b_n^t) . The spherical Bessel functions ($q = 1$) are chosen for convergence at the origin. $k_1 = n_1 k_0$ is the wave vector inside the core.

The main modification to the original Mie theory is the field in the spherical shell ($R_1 < r < R_2$). Since the convergence requirements at the origin (for “transmitted” field) and infinity (for “reflected” field) are absent in the shell, two types of Bessel functions need to be included. Here we choose the spherical Bessel functions ($q = 1$, associated with superscript “ j ”) and spherical Neumann functions ($q = 2$, associated with superscript “ y ”), such that,

$$\mathbf{E}_s(\mathbf{r}, t) = E_0 e^{-i\omega t} \sum_{n=1}^{\infty} i^n \frac{2n+1}{n(n+1)} \left[a_n^j \mathbf{m}_{o1n}^{(1)}(k_2 \mathbf{r}) + a_n^y \mathbf{m}_{o1n}^{(2)}(k_2 \mathbf{r}) - i b_n^j \mathbf{n}_{e1n}^{(1)}(k_2 \mathbf{r}) - i b_n^y \mathbf{n}_{e1n}^{(2)}(k_2 \mathbf{r}) \right] \quad (\text{S7a})$$

$$\mathbf{H}_s(\mathbf{r}, t) = -\frac{k_2 E_0}{\omega} e^{-i\omega t} \sum_{n=1}^{\infty} i^n \frac{2n+1}{n(n+1)} \left[b_n^j \mathbf{m}_{e1n}^{(1)}(k_2 \mathbf{r}) + b_n^y \mathbf{m}_{e1n}^{(2)}(k_2 \mathbf{r}) + i a_n^j \mathbf{n}_{o1n}^{(1)}(k_2 \mathbf{r}) + i a_n^y \mathbf{n}_{o1n}^{(2)}(k_2 \mathbf{r}) \right], \quad (\text{S7b})$$

with undetermined coefficients $(a_n^j, a_n^y, b_n^j, b_n^y)$. $k_2 = n_2 k_0$ is the wave vector inside the shell.

Determining the total field in Eq. (S2) requires solving for the set of coefficients $(a_n^r, a_n^j, a_n^y, a_n^t, b_n^r, b_n^j, b_n^y, n_n^t)$ by applying the boundary conditions at two surfaces,

$$\begin{aligned} \hat{\mathbf{r}} \times [\mathbf{E}_i(\mathbf{r}, t) + \mathbf{E}_r(\mathbf{r}, t)] &= \hat{\mathbf{r}} \times \mathbf{E}_s(\mathbf{r}, t) \\ \hat{\mathbf{r}} \times [\mathbf{H}_i(\mathbf{r}, t) + \mathbf{H}_r(\mathbf{r}, t)] &= \hat{\mathbf{r}} \times \mathbf{H}_s(\mathbf{r}, t) \end{aligned} \Big|_{r=R_2} \quad (\text{S8a})$$

$$\begin{aligned} \hat{\mathbf{r}} \times \mathbf{E}_s(\mathbf{r}, t) &= \hat{\mathbf{r}} \times \mathbf{E}_t(\mathbf{r}, t) \\ \hat{\mathbf{r}} \times \mathbf{E}_s(\mathbf{r}, t) &= \hat{\mathbf{r}} \times \mathbf{H}_t(\mathbf{r}, t) \end{aligned} \Big|_{r=R_1} \quad (\text{S8b})$$

Plugging Eqs. (S3), (S5), (S7), and (S6) into Eqs. (S8) and comparing each order of n yields,

$$\begin{aligned} \hat{\mathbf{r}} \times [\mathbf{m}_{o1n}^{(1)}(k_0\mathbf{r}) + a_n^r \mathbf{m}_{o1n}^{(3)}(k_0\mathbf{r}) - i\mathbf{n}_{e1n}^{(1)}(k_0\mathbf{r}) - ib_n^r \mathbf{n}_{e1n}^{(3)}(k_0\mathbf{r})] \\ = \hat{\mathbf{r}} \times [a_n^j \mathbf{m}_{o1n}^{(1)}(k_2\mathbf{r}) + a_n^y \mathbf{m}_{o1n}^{(2)}(k_2\mathbf{r}) - ib_n^j \mathbf{n}_{e1n}^{(1)}(k_2\mathbf{r}) - ib_n^y \mathbf{n}_{e1n}^{(2)}(k_2\mathbf{r})] \end{aligned} \Big|_{r=R_2} \quad (\text{S9a})$$

$$\begin{aligned} \hat{\mathbf{r}} \times k_0 [\mathbf{m}_{e1n}^{(1)}(k_0\mathbf{r}) + b_n^r \mathbf{m}_{e1n}^{(3)}(k_0\mathbf{r}) + i\mathbf{n}_{o1n}^{(1)}(k_0\mathbf{r}) + ia_n^r \mathbf{n}_{o1n}^{(3)}(k_0\mathbf{r})] \\ = \hat{\mathbf{r}} \times k_2 [b_n^j \mathbf{m}_{e1n}^{(1)}(k_2\mathbf{r}) + b_n^y \mathbf{m}_{e1n}^{(2)}(k_2\mathbf{r}) + ia_n^j \mathbf{n}_{o1n}^{(1)}(k_2\mathbf{r}) + ia_n^y \mathbf{n}_{o1n}^{(2)}(k_2\mathbf{r})] \end{aligned} \Big|_{r=R_2} \quad (\text{S9b})$$

$$\begin{aligned} \hat{\mathbf{r}} \times [a_n^j \mathbf{m}_{o1n}^{(1)}(k_2\mathbf{r}) + a_n^y \mathbf{m}_{o1n}^{(2)}(k_2\mathbf{r}) - ib_n^j \mathbf{n}_{e1n}^{(1)}(k_2\mathbf{r}) - ib_n^y \mathbf{n}_{e1n}^{(2)}(k_2\mathbf{r})] \\ = \hat{\mathbf{r}} \times [a_n^t \mathbf{m}_{o1n}^{(1)}(k_1\mathbf{r}) - ib_n^t \mathbf{n}_{e1n}^{(1)}(k_1\mathbf{r})] \end{aligned} \Big|_{r=R_1} \quad (\text{S9c})$$

$$\begin{aligned} \hat{\mathbf{r}} \times k_2 [b_n^j \mathbf{m}_{e1n}^{(1)}(k_2\mathbf{r}) + b_n^y \mathbf{m}_{e1n}^{(2)}(k_2\mathbf{r}) + ia_n^j \mathbf{n}_{o1n}^{(1)}(k_2\mathbf{r}) + ia_n^y \mathbf{n}_{o1n}^{(2)}(k_2\mathbf{r})] \\ = \hat{\mathbf{r}} \times k_1 [b_n^t \mathbf{m}_{e1n}^{(1)}(k_1\mathbf{r}) + ia_n^t \mathbf{n}_{o1n}^{(1)}(k_1\mathbf{r})] \end{aligned} \Big|_{r=R_1} \quad (\text{S9d})$$

Since the above equations must hold for all angles θ and ϕ , we find eight linear equations for the eight undetermined coefficients $(a_n^r, a_n^j, a_n^y, a_n^t, b_n^r, b_n^j, b_n^y, n_n^t)$,

$$j_n(k_0R_2) + a_n^r h_n^{(1)}(k_0R_2) = a_n^j j_n(k_2R_2) + a_n^y y_n(k_2R_2) \quad (\text{S10a})$$

$$\frac{[k_0R_2 j_n(k_0R_2)]'}{k_0R_2} + b_n^r \frac{[k_0R_2 h_n^{(1)}(k_0R_2)]'}{k_0R_2} = b_n^j \frac{[k_2R_2 j_n(k_2R_2)]'}{k_2R_2} + b_n^y \frac{[k_2R_2 y_n(k_2R_2)]'}{k_2R_2} \quad (\text{S10b})$$

$$k_0 j_n(k_0R_2) + b_n^r k_0 h_n^{(1)}(k_0R_2) = b_n^j k_2 j_n(k_2R_2) + b_n^y k_2 y_n(k_2R_2) \quad (\text{S10c})$$

$$k_0 \frac{[k_0R_2 j_n(k_0R_2)]'}{k_0R_2} + a_n^r k_0 \frac{[k_0R_2 h_n^{(1)}(k_0R_2)]'}{k_0R_2} = a_n^j k_2 \frac{[k_2R_2 j_n(k_2R_2)]'}{k_2R_2} + a_n^y k_2 \frac{[k_2R_2 y_n(k_2R_2)]'}{k_2R_2} \quad (\text{S10d})$$

$$a_n^j j_n(k_2R_1) + a_n^y y_n(k_2R_1) = a_n^t j_n(k_1R_1) \quad (\text{S10e})$$

$$b_n^j \frac{[k_2R_1 j_n(k_2R_1)]'}{k_2R_1} + b_n^y \frac{[k_2R_1 y_n(k_2R_1)]'}{k_2R_1} = b_n^t \frac{[k_1R_1 j_n(k_1R_1)]'}{k_1R_1} \quad (\text{S10f})$$

$$b_n^j k_2 j_n(k_2R_1) + b_n^y k_2 y_n(k_2R_1) = b_n^t k_1 j_n(k_1R_1) \quad (\text{S10g})$$

$$a_n^j k_2 \frac{[k_2R_1 j_n(k_2R_1)]'}{k_2R_1} + a_n^y k_2 \frac{[k_2R_1 y_n(k_2R_1)]'}{k_2R_1} = a_n^t k_1 \frac{[k_1R_1 j_n(k_1R_1)]'}{k_1R_1} \quad (\text{S10h})$$

These equations uniquely specify the undetermined coefficient for each order n . Solving Eqs. (S10) for these variables using any linear algebra package thus gives the full solution of the total field in Eq. (S2).

This method can further be generalized to core-shell structures with more than one layer of shells. For each additional layer, four undetermined coefficients and one additional set of surface-matching conditions need to be included, adding four more linear equations in Eqs. (S10).

**SUPPLEMENTARY NOTE 4: DISCUSSION OF THE FIELD ENHANCEMENT UNCERTAINTY
CAUSED BY THE MANUFACTURING SIZE DISPERSITY**

In Fig. ??a and Fig. ??d-f of the main text, we demonstrated the field enhancement for core-shell structures, with an uncertainty (red shaded area) caused by the manufacturing size dispersity. To be specific, the core-shell structures used in the experiment have an outer diameter of $D_2 = 147 \pm 7$ nm and an inner diameter of $D_1 = 118 \pm 4$ nm. This dispersity causes a rather large variation in the field enhancement. Here, we use Fig. ??d as an example to illustrate how this variation is addressed.

In Fig. S2, the dashed line is the field enhancement $|\alpha|^2$ simulated for $D_2 = 147 - 7$ nm and $D_1 = 118 + 4$ nm, where the shell thickness is the thinnest within the manufacturing dispersity. In this case, the peak field enhancement ($|\alpha|^2 \sim 110$) is obtained at approximately 700 nm. On the other extreme, for $D_2 = 147 + 7$ nm and $D_1 = 118 - 4$ nm, where the shell is the thickest, the peak field enhancement is significantly lower (~ 40), and the position is blue-shifted to approximately 610 nm. It is clear that the field-enhancement profile is the closest to that of the solid Au nanospheres of the same size when the shell thickness is the thickest possible within the manufacturing dispersity.

Since the small manufacturing dispersity causes pronounced differences in the field enhancement (almost 3 times in peak height and a blue shift of ≈ 90 nm), it is inaccurate to show just *one* line of field enhancement for a particular combination of outer and inner radii. Instead, at each wavelength, we calculated the range of field enhancement for all possible combinations of outer and inner radii within the manufacturing dispersity (shown as the red shaded area in Fig. S2) and highlight the average value (shown as the red circled line). In contrast to core-shell structures, our simulation shows that the same uncertainty for solid Au nanospheres is negligible.

Supplementary References

-
- [1] J. A. Powell, A. M. Summers, Q. Liu, S. J. Robotjazi, P. Rupp, J. Stierle, C. Trallero-Herrero, M. F. Kling, and A. Rudenko, *Opt. Express* **27**, 27124 (2019).
- [2] P. Rosenberger, P. Rupp, R. Ali, M. S. Alghabra, S. Sun, S. Mitra, S. A. Khan, R. Dagar, V. Kim, M. Iqbal, J. Schötz, Q. Liu, S. K. Sundaram, J. Kredel, M. Gallei, C. Costa-Vera, B. Bergues, A. S. Alnaser, and M. F. Kling, *ACS Photonics* **7**, 1885 (2020).
- [3] F. Süßmann, L. Seiffert, S. Zharebtsov, V. Mondes, J. Stierle, M. Arbeiter, J. Plenge, P. Rupp, C. Peltz, A. Kessel, S. A. Trushin, B. Ahn, D. Kim, C. Graf, E. Rühl, M. F. Kling, and T. Fennel, *Nature Communications* **6**, 7944 (2015).
- [4] S. Zharebtsov, T. Fennel, J. Plenge, E. Antonsson, I. Znakovskaya, A. Wirth, O. Herrwerth, F. Süßmann, C. Peltz, I. Ahmad, S. A. Trushin, V. Pervak, S. Karsch, M. J. J. Vrakking, B. Langer, C. Graf, M. I. Stockman, F. Krausz, E. Rühl, and M. F. Kling, *Nature Physics* **7**, 656 (2011).
- [5] G. Mie, *Annalen der Physik* **330**, 377 (1908).
- [6] J. Stratton, *Electromagnetic theory*, Vol. 33 (Wiley, 2007).